SUPPLEMENTAL MATERIAL for:

Unidirectional Transition Waves in Bistable Lattices
by N. Nadkarni, A. F. Arrieta, C. Chong, D. M. Kochmann, C. Daraio

---

1 Snapshot of the transition wave

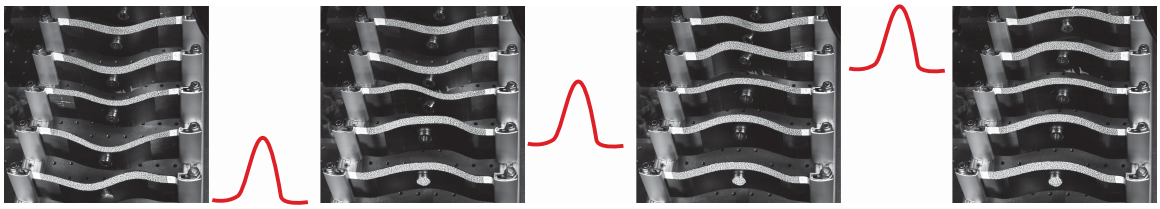

Figure 1: Snap-shot sequence showing the transition wave as it propagates through the experimental lattice. Images were acquired at 4000 fps. As can be seen, the wave is highly localized to a few elements.

2 Theoretical derivation of the continuum model

Consider the infinite nonlinear lattice with on-site (bistable) and inter-site nonlinearities with governing equation,

$$mu_{n,tt} + A(u_{n+1} - u_n + L)^p - A(u_n - u_{n-1} + L)^p + \alpha u_{n,t} + \beta\phi'(u_n) = 0. \tag{1}$$

where L is the lattice parameter and $p < -1$. We can therefore deduce the following relations:

1. The mass density should be a constant: $m/L = \text{constant} \Rightarrow m = O(L)$.
2. The energy density of the nonlinear spring should be constant: $-\frac{A}{p+1}\left(u_{n+1} - u_n + L\right)^{p+1}/L = -\frac{A}{p+1}\left(L\epsilon + L\right)^{p+1}/L = \text{constant} \Rightarrow A = O(L^{-p})$ where $\epsilon \sim O(1)$.
3. The energy density of the bistable function should be constant: $\beta\phi'(u_n)/L = \text{constant} \Rightarrow \beta = O(L)$.
4. The dissipation potential density should be a constant: $\frac{1}{2}\alpha u_{n,t}^2/L = \text{constant} \Rightarrow \alpha = O(L)$.

Assuming a traveling wave solution of the form, $u_n(t) = u(nL - vt) = u(\xi)$ gives

$$mv^2 u_{\xi\xi} + A\left(u(\xi + L) - u(\xi) + L\right)^p - A\left(u(\xi) - u(\xi - L) + L\right)^p - v\alpha u_\xi + \beta\phi'(u) = 0. \tag{2}$$

Using appropriate Taylor expansions for $u(\xi + L)$ and $u(\xi - L)$ results in

$$mv^2 u_{\xi\xi} + AL^p\left(1 + u_\xi + \tfrac{L}{2}u_{\xi\xi} + ...\right)^p - AL^p\left(1 + u_\xi - \tfrac{L}{2}u_{\xi\xi} + ...\right)^p - v\alpha u_\xi + \beta\phi'(u) = 0. \tag{3}$$

If we analyze the inter-element forcing function in the continuum limit, we obtain

$$F = -AL^p\left(1 + u_\xi + \tfrac{L}{2}u_{\xi\xi} + ...\right)^p. \tag{4}$$

The negative sign is required because the external force is compressive. As $L \to 0$, $AL^p \to k \sim O(1)$, giving,

$$F = -k\,(1+u_\xi)^p \tag{5}$$

As $p < -1$, for (5) to make physical sense, we need to the force to be finite which implies that $1+u_\xi \neq 0$. Referring back to the governing equation, we can perform another Taylor expansion in the continuum limit ($L \to 0$) so that

$$\begin{aligned} mv^2u_{\xi\xi} + AL^p\left((1+u_\xi)^p + \tfrac{L}{2}p\,u_{\xi\xi}(1+u_\xi)^{p-1} + ...\right) - AL^p\left((1+u_\xi)^p - \tfrac{L}{2}p\,u_{\xi\xi}(1+u_\xi)^{p-1} + ...\right) \\ - v\alpha u_\xi + \beta\phi'(u) = 0. \end{aligned} \tag{6}$$

Dividing throughout by L and rearranging gives

$$\begin{aligned} &\rho v^2u_{\xi\xi} + \tfrac{AL^{p+1}}{L}\left(p\,u_{\xi\xi}(1+u_\xi)^{p-1}\right) + \tfrac{AL^{p+3}}{L}[\tfrac{1}{6}(p-1)pu_{\xi\xi}u_{\xi\xi\xi}(u_\xi+1)^{p-2} + \\ &\tfrac{1}{24}(p-2)(p-1)pu_{\xi\xi}^3(u_\xi+1)^{p-3} + \tfrac{1}{12}pu_{\xi\xi\xi\xi}(u_\xi+1)^{p-1}] - v\tfrac{\alpha}{L}u_\xi + \tfrac{\beta}{L}\phi'(u) = 0. \end{aligned} \tag{7}$$

We can see that, $m/L = \rho \sim O(1)$, $-ApL^p = \rho c_0^2 \sim O(1)$, $\alpha/L = \gamma \sim O(1)$ and $\beta/L \sim O(1)$. Define $\frac{\beta}{L}\phi'(u) = \psi'(u)$. Taking the limit with respect to L (while keeping $O(L^2)$ terms), we obtain the continuum equation

$$\begin{aligned} &\rho v^2u_{\xi\xi} - \rho c_0^2\,u_{\xi\xi}(1+u_\xi)^{p-1} - \tfrac{1}{24}L^2\rho c_0^2[4(p-1)u_{\xi\xi}u_{\xi\xi\xi}(u_\xi+1)^{p-2} \\ &+ (p-2)(p-1)u_{\xi\xi}^3(u_\xi+1)^{p-3} + 2u_{\xi\xi\xi\xi}(u_\xi+1)^{p-1}] - v\gamma u_\xi + \psi'(u) = 0. \end{aligned} \tag{8}$$

Multiplying by u_ξ and integrating from $-\infty$ to ∞, we obtain

$$\begin{aligned} &-\tfrac{1}{24}L^2\rho c_0^2\int_{-\infty}^{\infty}[4(p-1)u_{\xi\xi}u_{\xi\xi\xi}(u_\xi+1)^{p-2} + (p-2)(p-1)u_{\xi\xi}^3(u_\xi+1)^{p-3} + 2u_{\xi\xi\xi\xi}(u_\xi+1)^{p-1}]u_\xi d\xi \\ &+ \int_{-\infty}^{\infty}\left(\rho v^2 - \rho c_0^2\,(1+u_\xi)^{p-1}\right)u_\xi u_{\xi\xi}d\xi + \int_{-\infty}^{\infty}\psi'(u)u_\xi d\xi = v\gamma\int_{-\infty}^{\infty}u_\xi^2\,d\xi. \end{aligned} \tag{9}$$

Now, as the system is dissipative, it is fair to assume that, as $t \to \infty$ or $\xi \to -\infty$, all derivatives of u go to zero. Also, as the system is initially at rest, all derivatives vanish as $t \to -\infty$ or $\xi \to \infty$. With this in mind, we review the second integral in (9). If the integration variable is rewritten using $u_{\xi\xi}d\xi = d(u_\xi)$ and $w = u_\xi$, we get

$$\int_{-\infty}^{\infty}\left(\rho v^2 - \rho c_0^2\,(1+u_\xi)^{p-1}\right)u_\xi u_{\xi\xi}d\xi = \int_{w(\xi\to-\infty)}^{w(\xi\to\infty)}\left(\rho v^2 - \rho c_0^2\,(1+w)^{p-1}\right)wdw = 0, \tag{10}$$

as $1+w \neq 0$, as proved earlier. Next, let us analyze the second term in the first integral (without the constant $-\frac{1}{24}L^2c_0^2$) in (9) and integrate by parts,

$$\begin{aligned} \int_{-\infty}^{\infty}[(p-1)(p-2)(u_\xi+1)^{p-3}u_{\xi\xi}][u_{\xi\xi}^2u_\xi]d\xi = &-2\int_{-\infty}^{\infty}(p-1)(u_\xi+1)^{p-2}u_{\xi\xi}u_\xi u_{\xi\xi\xi}d\xi \\ &- \int_{-\infty}^{\infty}(p-1)(u_\xi+1)^{p-2}u_{\xi\xi}^3d\xi. \end{aligned} \tag{11}$$

Performing a similar integration by parts on the last term of the first integral in (9), we obtain

$$\begin{aligned} 2\int_{-\infty}^{\infty}u_{\xi\xi\xi\xi}(u_\xi+1)^{p-1}u_\xi d\xi = &-2\int_{-\infty}^{\infty}(p-1)(u_\xi+1)^{p-2}u_\xi u_{\xi\xi}u_{\xi\xi\xi}d\xi \\ &+ \int_{-\infty}^{\infty}(p-1)(u_\xi+1)^{p-2}u_{\xi\xi}^3d\xi. \end{aligned} \tag{12}$$

Therefore, all the terms of the first integral will cancel each other. Similarly, if $u(\xi \to \infty) = u_i$ and $u(\xi \to -\infty) = u_f$, and without loss of generality, if $v > 0$, then (9) becomes

$$\int_{-\infty}^{\infty} \psi'(u) u_\xi d\xi = \int_{\psi(u_f)}^{\psi(u_i)} d(\psi(u)) = \psi(u_i) - \psi(u_f) = v\gamma \int_{-\infty}^{\infty} u_\xi^2 \, d\xi \geq 0 \Rightarrow \boxed{\psi(u_i) \geq \psi(u_f)} \quad (13)$$

3 Experimental force characterization

The magnetic force and bistable snapping force measurements were made using a Zwick-Roell compression testing machine. For measuring the magnetic interaction force, one of the magnets was kept fixed at the base of the machine while the other was fixed to the moving tip of the machine. A schematic of the experimental setup is shown in Fig. 1. The tip was moved downward at a constant rate of 20 mm/min and the force on the tip was recorded by the machine. A similar

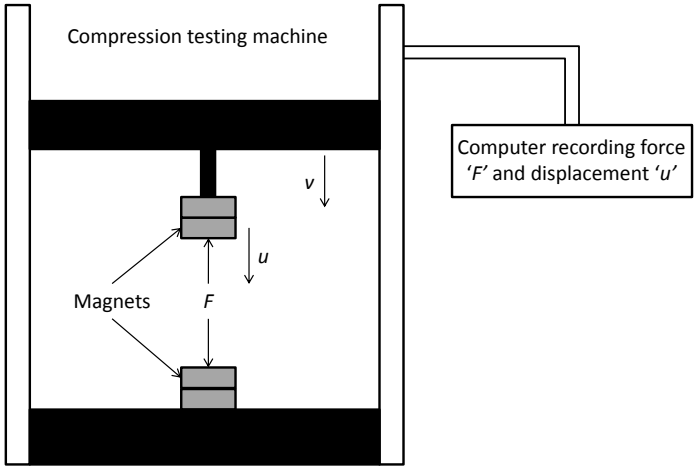

Figure 2: Schematic of maximum bistable force measurement

test was conducted for measuring the snapping force of the bistable composite. A schematic of the experiment is shown in Fig. 2. The element was held fixed, while the magnet on the machine tip was used to provide a non-contact force so as to allow the element to deform freely. In this experiment as well, the tip was moved downward at a constant rate of 20 mm/min.

4 Experimental details

A novel composite design featuring a spatially varying fiber distribution is utilized to produce bistable members with a tailored strain potential topology. This is comprised of a central [0/90] unsymmetrically laminated section surrounded by two transition sections, as shown in Fig. 4. The proposed lamination distribution allows for tailoring the depths of the potential wells and associated snapping forces, while enabling clamping the short edges. The dimensions for the elements used in the model demonstrator used in the main manuscript are given in table 1. Table 2 provides the material properties of the used c-m-p (CM-Preg T-C-120/625 CP002 35) prepreg system. It

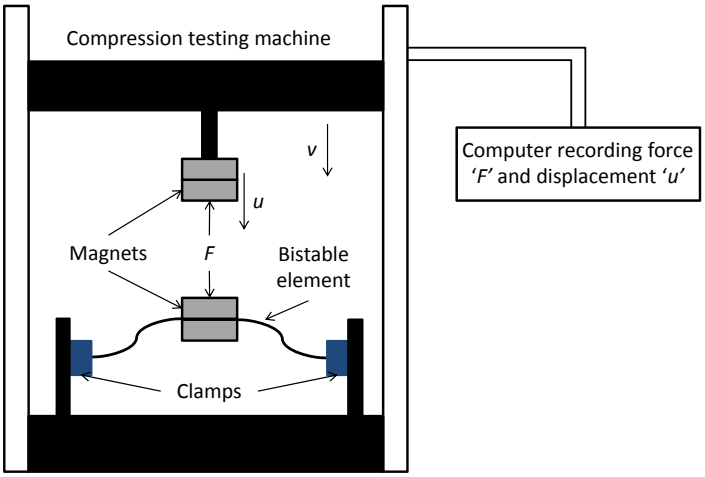

Figure 3: Schematic of maximum bistable force measurement

is worth mentioning that the dimensions of the regions making up the fibre distribution of this laminates can provide a very broad range of different potential wells and snapping forces as detailed in Ref. [1]. The magnets were of the R-19-09-06 N type (mass of 10 g, inner diameter 9.5 mm,

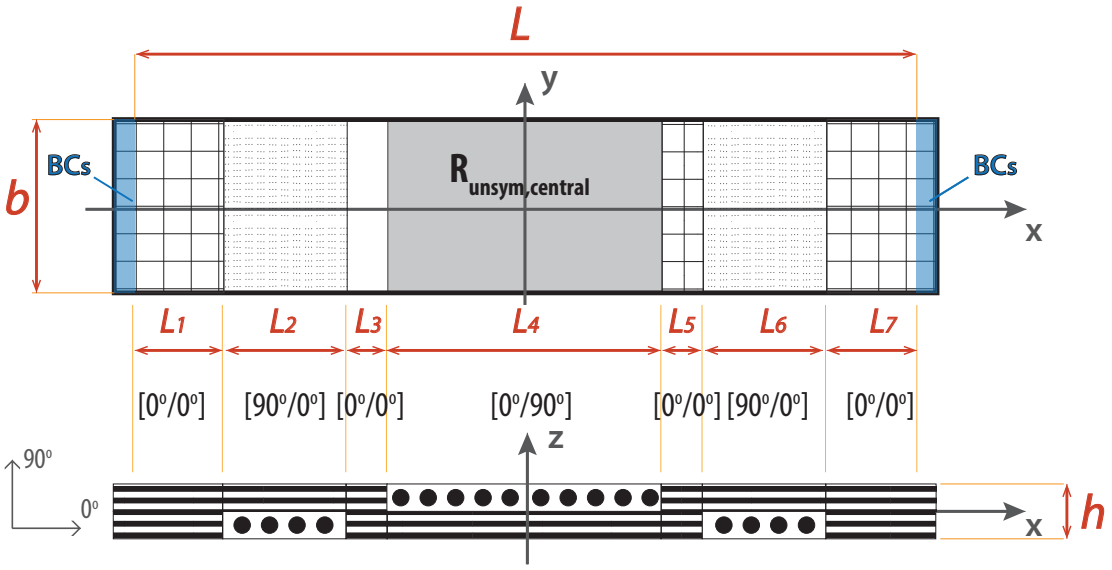

Figure 4: Tailored distribution of used bistable composite laminates.

outer diameter 19.1 mm and thickness of 6.4 mm), supplied by Supermagnete. The experiments were performed with two Photron Ux 100 cameras, using a Digital Image Correlation system from Correlated Solutions.

L [mm]	b [mm]	h [mm]	L_1 [mm]	L_2 [mm]	L_3 [mm]	L_4 [mm]	L_5 [mm]	L_6 [mm]	L_7 [mm]
220	64	0.25	31	15	5.0	120	5.0	15	31

Table 1: Geometric properties of the sections composing the spatially varying fiber for the bistable elements. Refer to for the schematic representation in Fig. 4 of the given parameters.

Material	Fibre vol. [%]	E_{11} [GPa]	E_{22} [GPa]	G_{12} [GPa]	ν_{12} [-]	ρ $[\frac{\text{kg}}{\text{m}^3}]$	α_{11} K^{-1}	α_{22}
CFRP	60	161	10	4.4	0.3	1570	-1.8E-8	2.25E-5

Table 2: Material properties for a typical ply of CFRP c-m-p (CM-Preg T-C-120/625 CP002 35) prepreg used to manufacture the bistable elementsly. Nominal prepreg thickness 0.125 mm.

5 Numerical simulations for exact traveling waves

Transition waves of Eq. (1) (of the manuscript) correspond to orbits of Eq. (2) (of the manuscript) that connect the equilibrium $u = u_i$ and $u = u_f$ where u_i and u_f are the positions of the potential wells of $\beta\phi$. Such special orbits of advance-delay equations, like Eq. (2) (of the manuscript), can be approximated numerically up to a prescribed tolerance [2]. In particular, one can make the discretization $u^j := u(j\Delta\xi)$ where $j \in \mathbb{Z}$ which, upon a choice of finite difference approximation of the derivatives, results in an algebraic equation that can be solved via Newton iterations:

$$\begin{aligned} v^2 m \frac{u^{j+1} - 2u^j + u^{j-1}}{\Delta\xi^2} - v\alpha \frac{u^{j+1} - u^{j-1}}{2\Delta\xi} + \beta\phi'(u^j) \\ + A(u^{j+q} - u^j + L)^p - A(u^j - u^{j-q} + L)^p = 0, \end{aligned} \tag{14}$$

where $\Delta\xi$ is chosen such that $q = L/\Delta\xi$ is an integer. We impose no flux boundary conditions and let the wave velocity v be a variable of the system (rather than a fixed parameter). We found that despite varying the initial guess, our algorithm converges to the same profile and wave velocity v, implying that for a fixed set of system parameters, there is a unique wave velocity of the transition wave.

6 Robustness analysis

6.1 Sensitivity of wave velocity with respect to interaction coefficient

Fig. 5 shows the variation of the wave velocity for various coefficients of the interaction potential (parameter p of Eq. (1) in the manuscript). It can be seen that the velocity becomes zero beyond a certain critical value of the parameter p. From a physical point of view this is reasonable.The strength of inter-element forcing decreases with decreasing nonlinearity parameter p. When the initial element is snapped over, the small force due to magnetic coupling not sufficient for the subsequent element to snap over the on-site potential energy barrier, thereby causing the wave to stagnate. This is analogous to the propagation failure observed in discrete reaction-diffusion

lattices [3]. The value of $p = -3.274$ in the experiments lies well above the critical range for each of the parameter values shown in Fig. 5. For a fixed lattice distance, the potential barrier decreases as the rail distance increases. Therefore, it is not surprising that the critical value of the nonlinearity p at which the wave stoppage occurs decreases as the rail distance increases, see Fig. 5(a). For a constant rail distance, as the lattice distance increases, the interaction force between magnets in the undeformed state decreases (since the distance between the magnets that couple the elements is increasing). Hence, the nonlinearity p at which the wave stops propagating increases as the lattice distance increases, see Fig. 5(b).

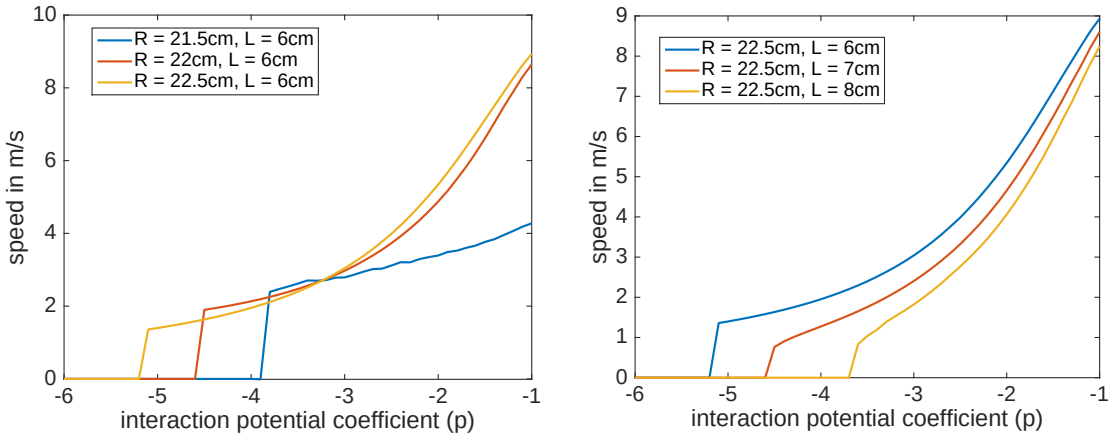

(a) (b)

Figure 5: (a) Variation of wave velocity with interaction coefficient p for different rail distances while keeping the lattice distance constant. (b) Variation of wave velocity with interaction coefficient p for different lattice distances while keeping the rail distance constant.

6.2 Sensitivity of wave velocity with respect to asymmetry of the on-site bistable potential

To obtain a theoretical approximation of the onsite potential $\psi(u)$ for the snapping elements, the experimentally measured values of the distance and corresponding force were fit by a polynomial spline (see Fig. 1a of the manuscript). To investigate the role of the asymmetry numerically we introduce an asymmetry parameter ϵ where $\epsilon = 0$ corresponds to the asymmetry of the experimentally measured on-site potential, and $\epsilon = 1$ corresponds to a symmetric potential (see Fig. 6(a) and text below for details). As an example, we consider a rail distance of $R = 22.5$ cm and a lattice spacing of $L = 8$ cm. We performed a parametric continuation of roots of Equation (3) of the main manuscript with respect to the asymmetry parameter ϵ. The corresponding value of the wave speed v is plotted against the asymmetry parameter ϵ in Fig. 6(b). Note the wave speed decreases as the asymmetry weakens. It appears that there is a threshold wave speed, since solutions cease to exist for a finite, non-zero value of the asymmetry parameter ϵ (about $\epsilon_{cr} = 0.754$). This is also in line with earlier observations that wave propagation is possible in the asymmetric lattice only. Indeed, we simulated the original equations of motion (1) with an asymmetry parameter above the critical value ϵ_{cr} (namely $\epsilon = 0.76$) and found that no wave propagation is possible. Using a value slightly below the bifurcation point (namely $\epsilon = 0.74$) led to a stable wave propagation.

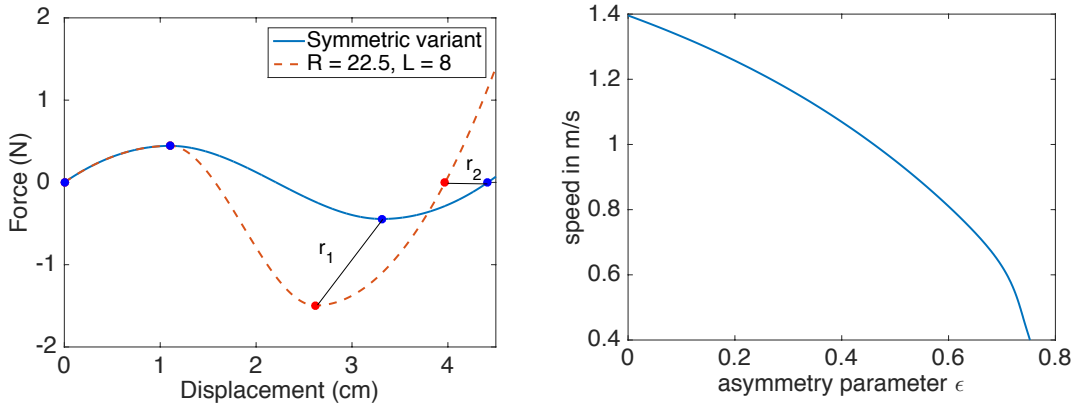

(a) (b)

Figure 6: (a) Fitted onsite force for the case of $R = 22.5$ cm and $L = 8$ cm (dashed red line) and experimentally measured values (red markers). The symmetric counterpart of this function is also shown (blue solid line), which was obtained by modifying the local minimum and largest root along the lines r_1 and r_2 respectively. The fraction of the distance moved along these lines is the asymmetry parameter ϵ. (b) Plot of the wave speed as the asymmetry parameter ϵ is varied.

Determination of the asymmetry parameter ϵ: Let the experimentally measured local minimum be (u_1, F_1), the local maximum be (u_2, F_2), and the largest root be $(u_3, 0)$, where the first entry of each of these coordinate pairs is the displacement and the second entry is the force (see red markers of Fig. 1a of the main manuscript and of Fig. 6(a)). To explore how the degree of asymmetry affects wave propagation, we modified the values of x_3 and (x_2, y_2) gradually until a symmetric function was obtained (see blue curve of Fig. 6(a)). The symmetric function of interest corresponds to the spline passing through the points $(0,0), (u_1, F_1), (3u_1, -F_1)$ and $(4u_1, 0)$ (the spline was determined with the same procedure used to obtain the solid line of Fig. 1a of the main manuscript). Let $r_1 = \sqrt{(u_2 - 3u_1)^2 + (F_2 + F_1)^2}$ be the distance between the experimentally measured local minimum (u_2, F_2) and the value $(3u_1, -F_1)$. Let $r_2 = \sqrt{(u_3 - 4u_1)^2}$ be the distance between the experimentally measured point $(u_3, 0)$ and the value $4u_1$. We then introduce an asymmetry parameter ϵ where $\epsilon = 0$ corresponds to the asymmetry of the experimentally measured onsite-potential and $\epsilon = 1$ corresponds to a symmetric potential. In particular we modify the values (u_2, F_2) and u_3 such that the distances r_1 and r_2 change like $r_1 \to r_1 - \epsilon r_1$ and $r_2 \to r_2 - \epsilon r_2$ for various values of $\epsilon \in [0, 1]$.

References

[1] Izabela K. Kuder, Andres F. Arrieta, and Paolo Ermanni. Design space of embeddable variable stiffness bi-stable elements for morphing applications. *Composite Structures*, 122:445 – 455, 2015. ISSN 0263-8223. URL `http://www.sciencedirect.com/science/article/pii/S0263822314006424`.

[2] H. Xu, P.G. Kevrekidis, and A. Stefanov. Traveling waves and their tails in locally resonant granular systems. *Journal of Physics A: Mathematical and Theoretical*, 48(19):195204, 2015. URL `http://stacks.iop.org/1751-8121/48/i=19/a=195204`.

[3] Thomas Erneux and Grégoire Nicolis. Propagating waves in discrete bistable reaction-diffusion systems. *Physica D: Nonlinear Phenomena*, 67(1-3):237–244, 1993.